Title
Fast ICCD-based temperature modulated fluorescence tomography.

Journal
Applied Optics, 62(28)

ISSN
1559-128X

Authors
Nouizi, Farouk
Kwong, Tiffany C
Turong, Bryan
et al.

Publication Date
2023-10-01

DOI
10.1364/ao.499281

Peer reviewed

Published in final edited form as:

Appl Opt. 2023 October 01; 62(28): 7420–7430. doi:10.1364/AO.499281.

Fast ICCD-based temperature modulated fluorescence tomography

Farouk Nouizi[1,2,*], **Tiffany C. Kwong**[1,3], **Bryan Turong**[1], **Deniz Nikkhah**[1], **Uma Sampathkumaran**[4], **Gultekin Gulsen**[1,2]

[1]Tu and Yuen Center for Functional Onco-Imaging, Department of Radiological Sciences, University of California, Irvine, California 92697, USA

[2]Chao Family Comprehensive Cancer Center, University of California, Irvine, California 92697, USA

[3]Natural Science Division, Pasadena City College, 1750 E. Colorado Blvd, Pasadena, California 91106, USA

[4]InnoSense LLC, 2531 West 237th Street, Suite 12, Torrance, California 90505, USA

Abstract

Fluorescence tomography (FT) has become a powerful preclinical imaging modality with a great potential for several clinical applications. Although it has superior sensitivity and utilizes low-cost instrumentation, the highly scattering nature of bio-tissue makes FT in thick samples challenging, resulting in poor resolution and low quantitative accuracy. To overcome the limitations of FT, we previously introduced a novel method, termed temperature modulated fluorescence tomography (TMFT), which is based on two key elements: (1) temperature-sensitive fluorescent agents (ThermoDots) and (2) high-intensity focused ultrasound (HIFU). The fluorescence emission of ThermoDots increases up to hundredfold with only several degree temperature elevation. The exceptional and reversible response of these ThermoDots enables their modulation, which effectively allows their localization using the HIFU. Their localization is then used as *functional a priori* during the FT image reconstruction process to resolve their distribution with higher spatial resolution. The last version of the TMFT system was based on a cooled CCD camera utilizing a step-and-shoot mode, which necessitated long total imaging time only for a small selected region of interest (ROI). In this paper, we present the latest version of our TMFT technology, which uses a much faster continuous HIFU scanning mode based on an intensified CCD (ICCD) camera. This new, to the best of our knowledge, version can capture the whole field-of-view (FOV) of 50 × 30 mm^2 at once and reduces the total imaging time down to 30 min, while preserving the same high resolution (~1.3mm) and superior quantitative accuracy (<7% error) as the previous versions. Therefore, this new method is an important step toward utilization of TMFT for preclinical imaging.

* fnouizi@uci.edu .

Disclosures. The authors declare no conflicts of interest.

1. INTRODUCTION

Fluorescence imaging has been widely used to study many disease models including cancer, mainly to study progression and pathology, response to therapy, receptor-targeted applications, and probe development [1–8]. However, most of the preclinical work based on diffuse optical fluorescence imaging is to a large extent done through 2D planar epi-illumination imaging, mainly by illuminating and imaging the animal from above [9]. In fact, the spatial resolution of planar images will vary considerably with depth of the fluorophore distribution due to the highly scattering and absorptive nature of the tissue [10]. This depth-dependent resolution is a ubiquitous trait of planar imaging mode. This limitation can be significantly reduced using trans-illumination mode, where the animal is illuminated and imaged from the opposite sides [11,12].

It is believed that orthotopic and transgenic tumor models using genetically engineered animals provide a more realistic platform for cancer imaging. Tumor cell interactions with the surrounding tissue stromal environment, including extracellular matrix, local enzymes and proteases, vasculature, inflammatory cells, growth factors, and hormones, can significantly affect tumor development [13–15]. However, they are extensively altered or even missing to a large extent when tumors are grown in ectopic environments such as skin [16,17]. Unfortunately, most orthotopic tumor models and especially spontaneous tumors cannot be successfully resolved by planar fluorescence imaging.

Fluorescence tomography (FT) is necessary for 3D imaging of orthotopic/transgenic tumor models. However, diffusion of light in highly scattering tissue makes FT very challenging. Despite the efforts of the community, FT still could not provide the desired spatial resolution and quantitative accuracy, hampering its widespread use in preclinical imaging. Hence, its advantages such as superior sensitivity and low-cost instrumentation are not harnessed adequately for 3D tomographic preclinical imaging. Extensive effort has been spent to improve its resolution by combining FT with other anatomic imaging modalities such as x-ray CT, MRI, and ultrasound [18–28]. Accordingly, structural *a priori* information is utilized to guide and constrain the fluorescence image reconstruction algorithm to improve its performance. However, this approach does not work well since the fluorophores cannot be localized in the anatomical images. Also, the fluorescence target boundaries do not always correlate with structural ones [29].

An alternative approach has been to modulate the fluorescence signal using other modalities in an interactive way. For example, focused ultrasound has been previously employed to modulate fluorescence signals by tagging the optical photons. In this approach, longitudinal vibrations created by a scanning ultrasound column are used to modulate the optical parameters of tissue. Since only the photons passing through the small ultrasound focal zone are tagged, selective detection of these photons improves the resolution of fluorescence imaging substantially. However, extremely low signal-to-noise ratio due to limited modulation depth of the optical signals generated by the ultrasound column makes this approach difficult to implement [30–32]. Microbubbles that are surface-loaded with self-quenching fluorophores have also been used to enhance the contrast for ultrasound tagging [33,34]. However, their disadvantages are their instability, low circulation residence

times, low binding efficiency to the area of interest especially in the fast-flow conditions, and possible side effects if destructed during imaging session [35,36].

We previously introduced a new imaging modality called temperature modulated fluorescence tomography (TMFT) [37–46]. This technique leverages the high resolution of ultrasound with the ultrahigh sensitivity of the fluorescence imaging. TMFT uses temperature dependence of special fluorescence contrast agents called “ThermoDots” together with the focused ultrasound to achieve thermal modulation with high spatial resolution. The idea is to scan focused heating zones over the imaging volume and localize the resulting variation in the fluorescence emission of ThermoDots. A focused ultrasound transducer is used to generate the localized hot spots (~1.3 mm in diameter). With the help of the focused hot spot, TMFT can resolve the spatial distribution of the ThermoDots with high resolution. The spatial resolution is determined by the spot size of the HIFU (~1.3 mm), which is not possible to achieve with conventional fluorescent tomography techniques. Moreover, TMFT spatial resolution is preserved up to a depth of 60 mm depending on the type of the HIFU transducer.

The activatable properties of ThermoDots are dependent on two main ingredients: ICG and pluronic polymers [47–49]. Their key advantage is that their fluorescence signal intensity and lifetime are drastically temperature dependent [38]. Indeed, only 4 degree temperature elevation increases the fluorescent emission of ThermoDots up to hundredfold. However, only a couple degrees of local temperature elevation are enough since the full hundredfold fluorescent signal is not necessary for detecting the change in the detected signal. Meanwhile, the local heating is achieved by focusing acoustic waves in a focal zone utilizing a high-intensity focused ultrasound (HIFU) transducer. Therefore, TMFT is based on a novel way of synergetic integration of two modalities: ultrasound (HIFU) and optical imaging (FT).

During TMFT data acquisition, first, conventional FT is performed to determine region-of-interest (ROIs), where ThermoDots accumulate. Following that, the fluorescence signal is continuously monitored while scanning the HIFU over those ROIs. There is no change in the fluorescence signal in the absence of ThermoDots over the scanning area. However, a sudden increase in their emission signal is observed the moment HIFU scans over the target containing ThermoDots. Hence, a binary mask that exactly represents the distribution of ThermoDots within each ROI is obtained with high resolution. This binary map directly maps the distribution of ThermoDots and, thus, can be used as an accurate *functional a priori*, unlike *structural a priori* used in the conventional multimodality imaging methods leveraging anatomical imaging [37–46,49,50]. This is one of the main advantages of the TMFT technique.

Several other groups also have spent extensive efforts to improve the performance of the fluorescence imaging utilizing different temperature-sensitive fluorescent contrast agents but mostly in 2D planar imaging mode [51–54]. On the other hand, our focus has been on 3D imaging in tomographic mode. Our first attempts in the development of the TMFT were mainly fiber-based techniques, where optical fibers in contact with the tissue boundary were utilized to deliver excitation light and detect the emitted fluorescence signals [43,44,46,55].

This fiber-based configuration presented several critical limitations that hampered the translation of TMFT to *in vivo* small animal imaging. Mainly, the subject under investigation needed to be immersed in an optical matching liquid, and the number of source-detector pairs was limited by the number of optical fibers.

To alleviate these limitations, we recently developed a CCD camera-based TMFT system that was designed for small animal imaging [56–58]. In this configuration, the camera was placed above the subject under investigation to enable free-space detection. The animal was placed on top of an ultrasound transparent membrane, which supported and kept it in contact with the acoustic medium. Water was used as an acoustic medium for the HIFU scanned below the membrane. The output of the laser source was mounted onto the center of the HIFU transducer. This approach allowed illumination of the subject with a collimated laser beam from its bottom through water. Hence, this design was a big step toward *in vivo* small animal imaging with TMFT due to the user-friendly design that eliminated the difficult task of immersing the animal. Despite those improvements, the imaging time of this CCD-based system was relatively long. One of the main reasons was that the HIFU transducer was scanned in a step-and-shoot mode while the CCD collected signals with a long integration time at each step. Since step-and-shoot mode was very time consuming, it was not feasible to perform it over the whole FOV. Hence, performing conventional FT reconstruction in between data acquisition steps was necessary to identify one or more ROIs. Despite completing measurements on a limited area over a selected ROI, the total imaging time was still over an hour with the addition of the conventional FT reconstruction.

In this paper, we present a faster methodology to improve the CCD-based TMFT. To achieve higher data acquisition speed, we first upgraded the camera to an intensified CCD (ICCD). Having an intensifier stage with high gain, the ICCD allowed us to reduce the integration times from 2 s to 66 ms. This in turn allowed us to move from the step-and-shoot mode to a continuous scanning mode, where the ICCD recorded a series of images while the HIFU is continuously scanned over the whole FOV. This eliminated the delineation of each ROI from the conventional FT and time-consuming step-and-shoot TMFT measurement scheme. Indeed, this ICCD-based TMFT system achieved the same resolution as the previous version while keeping total imaging time below 30 min due to higher sensitivity of the ICCD. Furthermore, our industrial collaborators (InnoSense, Torrance, CA) extended the operating temperature range of the ThermoDots from 17–21°C to 30–34°C, which was a prerequisite for live animal imaging. We believe that these critical improvements finally pave the way for *in vivo* small animal imaging with TMFT.

2. MATERIALS AND METHODS

A. Contrast Agents (ThermoDots)

Three types of temperature-sensitive fluorescent probes have been reported in the literature [59]. These are, mainly, temperature-sensitive polymer nanoparticles [60], temperature-responsive micelles [38,61,62], and thermosensitive liposomes [63,64]. ThermoDots used in this study consist of temperature-responsive pluronic polymer-derived micelles encapsulating a near-infrared (NIR) imaging agent, indocyanine green (ICG). The hydrophobicity and hydrophilicity of the core and cornea of the micelle are temperature

dependent. Therefore, the solvent polarity varies with the local temperature, which results in a change in the quantum efficiency of the loaded ICG micelles. Just by modulating the environment temperature 4 deg, their quantum efficiency can be varied a hundredfold. This huge variation in the fluorescence emission allows their utilization as a fluorescent switch. Indeed, they emit stronger fluorescence signals when the locale temperature increases [47–49].

Our industrial collaborators previously synthesized ThermoDots with an operating thermal dynamic range designed around the average room temperature (17–23°C), Fig. 1 (a). These were very useful to test the TMFT prototypes in the lab with phantoms mimicking optical properties of small animals. For those, Pluronic-F127 polymer is used as the main ingredient, which consists of an amphiphilic tri-block copolymer of ethylene and propylene oxide that can self-assemble into a micelle in aqueous solution [8,9]. ThermoDots synthesized using Pluronic-F127 had a limited thermal range and perform only below 25°C. However, when animals are anesthetized, generally their body temperature stabilizes around 31°C. To adapt the operating temperature range for *in vivo* imaging, our collaborators tried several polymers and found out that ThermoDots synthesized using polymer F108 were more suited in the temperature range of 30–34°C. In that range, the fluorescence emission of the ThermoDots increased approximately a hundredfold as seen in Fig. 1 (b). Moreover, both versions of the ThermoDots were also PEGylated to make them ready for conjugating with antibodies. The future generation of disease-targeting ThermoDots based on antibodies will accumulate in the diseased area. Hence, these new ThermoDots based on the polymer F108 will be critical for future *in vivo* studies.

B. Instrumentation

As aforementioned, the first version of the TMFT was fiber-based. Light was routed into and from the imaging interface using optical fibers placed on each side of the phantom holder. The limited source-detector numbers restricted the size of the tomographic data collected in that scheme. In the next generation camera-based system, we utilized a CCD camera that collects considerable larger tomographic data due to coverage of the whole FOV and records an image for every HIFU position. Moreover, we coupled the collimated laser beam with the HIFU transducer and scanned them together. In fact, these two parts were decoupled in the fiber-based system (i.e., only the HIFU beam was moving). Most importantly, the camera-based approach allows the subject being imaged to be placed on an ultrasound transparent membrane and eliminates the necessity of the immersion of the subject to an optical matching medium.

We upgraded our previous CCD-based TMFT system using an ICCD (Stanford Photonics, Palo Alto, CA), Fig. 2(b). In this configuration, the animal is placed on a HIFU transparent membrane, and the camera is placed directly above it to enable free-space data collection. This configuration makes the system user friendly with high throughput. A 785 nm laser is used to excite the ThermoDots. The laser light is transferred to the TMFT system using an optical fiber. The output of the fiber is terminated with a fiber optic collimator, which is placed at the circular hole at the center of the HIFU transducer (H102, Sonic Concepts, Inc., Bothell, WA). This provides the ability to scan both the laser and the HIFU beams

together in tandem. The HIFU transducer has a focal length of ~60 mm and produces a cylindrical focal zone of ~1.3 mm in diameter and 10 mm in height. It is operated at 1.025 MHz utilizing a signal generator (33220A, Agilent Technologies) that is cascaded with a variable attenuator (355C, Agilent Technologies) and a 100 watt amplifier (155LCRH, Kalmus, USA). This combination allows for adjusting the HIFU power and limiting it to achieve only a couple of degrees local temperature elevation at the focal zone.

On the detection side, the ICCD camera provided much higher sensitivity owing to its intensifier stage. A computer-controlled filter wheel is placed in front of it to switch optical bandpass filters between fluorescence and absorption measurements. Fluorescence measurements are performed for conventional FT and TMFT. Meanwhile, the absorption measurements are used to obtain 3D absorption maps to improve the modeling of light propagation and, hence, FT reconstruction results [65]. Tissue-like agarose phantoms are utilized to test the system. ThermoDots are embedded inside of these rectangular phantoms, which are placed on top of the ultrasound and light transparent membrane. Figure 3(a) shows the top view of the imaging interface and the phantom upper surface.

Having a high-sensitivity ICCD in this new system accelerated the data acquisition scheme. As opposed to the step-and-shoot mode, the computer-controlled translation stages are used to continuously move the HIFU and collimated laser beam over the whole FOV in linear fashion. Meanwhile, images are dynamically acquired with the ICCD. When the ThermoDots are in the focal zone of the HIFU beam, their local temperature increases, which leads to higher fluorescence emission, Fig. 3(d). The continuous scanning method considerably reduces the imaging time. Before going into the details of the continuous scanning method, however, it is important to mention that coupling the motion of the HIFU and laser beam together brought up an important advantage for this approach, as explained in the next section.

C. Comparison of Performance for Coupled and Decoupled HIFU and Laser Beams

The fluorescence signal emitted by the ThermoDots depends both on the local excitation light photon density and the local temperature. When the HIFU and optical beams are decoupled, the HIFU beam is moving while the optical excitation beam is kept steady as seen in Fig. 4(a). That leads to a sudden increase in the detected fluorescence signal when traveling HIFU beam hits to the ThermoDots, causing an increase in the local temperature. However, the signal does not decrease immediately when the HIFU beam moves away from the inclusion where ThermoDots are located, indicated by the green area in Fig. 4. This is because of the relatively low heat transfer in the phantom preventing the local temperature to drop quickly. While the sudden increase allows us to detect the first edge of the target containing the ThermoDots, the slowly decreasing signal prevents us from determining the second edge of the target. Therefore, it is necessary to scan the FOV from both sides since only one edge of the inclusion containing ThermoDots can be determined during a linear scan. On top of that, postprocessing is necessary by taking derivatives of the signals to find the edges of the inclusion from both sides. The details can be found in our previous publication [44].

On the other hand, when the HIFU and laser beams are coupled, they are scanned together. In this scheme, the signal increases as soon as the ThermoDots are within the HIFU hot spot. However, the detected signal decreases right away as soon as the ultrasound beam moves away since the collimated laser beam is coupled with it and moving away from the target. Mainly, the quick reduction in the excitation photon density dominates since the laser beam is moving away, which causes instantaneous reduction in the emitted fluorescence signal despite elevated local temperature levels as seen in Fig. 4(b). Hence, both edges of the inclusion can be identified easily, and the requirement of the linear scan from opposite direction is eliminated together with extensive postprocessing as in the case of decoupled HIFU and laser beams.

D. Data Acquisition

At the beginning of the imaging session, the subject under investigation is placed on a thin membrane that is transparent for both optical and ultrasound waves. First, conventional optical tomography acquisition is completed in absorption and fluorescence mode, while HIFU is turned off For this purpose, the excitation laser beam (785 nm) is scanned from the bottom of membrane over a 8 × 5 grid using the translational stage. First, the excitation light is turned on at every grid position, and a conventional tomographic measurement is acquired with the ICCD providing a total of 40 images (1340 pixels × 1024 pixels). Integration time of the ICCD is kept at 100 ms. Including the positioning time, the total imaging time is less than 1 min for the absorption measurements. The absorption maps reconstructed using these measurements at the excitation wavelength of the ThermoDots are later used in the FT inverse solver to increase its accuracy [36]. Following that, an 830 ±10 nm bandpass filter is placed in front of the camera for fluorescence measurements. This bandpass filter helps eliminate the excitation light component in the detected light while passing only the fluorescence emission of the ThermoDots. The very same data acquisition procedure is repeated to acquire conventional FT measurements while increasing the integration time of the ICCD to 500 ms. The main reason is the weak fluorescence emission of the ThermoDots when the local temperature is low. Despite the increase in the integration time, the FT acquisition is completed in less than a minute.

Once the conventional optical tomography measurements are done, HIFU is turned on to complete the TMFT measurements. It is operated at low power mode yielding a heating of a few degrees for a short period of time. During the TMFT HIFU scanning, two orthogonal scans are performed, in x and y directions. Scans are performed over several 1.3-mm-wide lines to cover the whole FOV in both x and y directions. Each line-scan is acquired twice, with the HIFU power turned off, then turned on. The former one is used as a baseline and subtracted from the latter one to calculate the difference that is only due to the increase in the emission of ThermoDots at an elevated local temperature. To be able to compare the signals, an ROI is determined (50% of the maximum signal) in the ICCD images. The intensity of the pixels inside this ROI is integrated for each image. Since images are acquired in a dynamic fashion with ICCD during HIFU scan, each image corresponds to a different HIFU position on the line-scan.

Figure 4(b) shows the resulting difference profile along the line-scan going through the target filled with ThermoDots. In the absence of ThermoDots along the scanning line of the active HIFU beam, no change in the fluorescence signal is observed. However, there is a sudden signal increase when the HIFU scans over the target. Once the HIFU beam leaves the target, the fluorescence signal starts decreasing quickly as explained in the previous section. One side of the fluorescence target boundary is identified by a significant increase in the signal. The other side is identified when the signal decreases more than 30% compared to the previous time point that corresponds to the moment when the HIFU and laser beam leaves the object together, Fig. 4(b). At the end, a binary map is created for x and y scans, separately. Following that, these two maps are first multiplied and then segmented at full width at half-maximum (FWHM) to create a final binary mask [44]. In fact, this binary mask already represents a high-resolution map of the true localization of ThermoDots in the tissue, which is later used as *"functional a priori"* during the FT image reconstruction process [44].

E. TMFT Image Reconstruction Algorithm

The mathematical framework for TMFT follows the conventional FT. First, the propagation of the excitation light is modeled from the tissue entrance point to the target containing fluorophores. After that, the fluorescence emission light is modeled from the target to the surface of the medium using the coupled diffusion equation [66–70]. During this process, the quantum efficiency is used to model the thermally dependent fluorescence emission as a function of local temperature, $\eta(T)$, at the right-hand side of the second equation of Eq. (1). Therefore, the modified TMFT forward problem permits calculating the density of emission photons, Φ_m^T, generated by the ThermoDots at temperature T [37,44],

$$\begin{cases} \nabla\left[D_x \nabla \Phi_x(r)\right] - (\mu_{ax} + \mu_{af})\Phi_x(r) = -q_0(r) \\ \nabla\left[D_x \nabla \Phi_m^T(r)\right] - \mu_{am}\Phi_m^T(r) = -\Phi_x(r)\eta(T)\mu_{af} \end{cases}, \tag{1}$$

where $\mu_{af} = 2.303 \cdot \varepsilon \cdot C$ is the absorption coefficient of fluorescence, with ε and C being, respectively, the molecular extinction coefficient and the concentration of the fluorophore. $\Phi_x(r)$ is the excitation photon density. The diffusion coefficient is defined by $D = \frac{1}{3(\mu_a + \mu_s')}$, with μ_a and μ_s' being, respectively, the absorption and reduced scattering coefficients of the medium [44,71]. The subscripts x and m represent the excitation and the emission wavelengths, respectively.

To reconstruct the TMFT images, an inverse problem is solved by minimizing the difference between the fluorescence fluence measured at the surface of the medium and the one calculated by solving Eq. (1),

$$\Omega(\mu_{af}) = \sum_{i=1}^{N_s} \sum_{j=1}^{N_d} \left(\Im_{ij}^T - F_{ij}^T(\mu_{af})\right)^2, \tag{2}$$

where $\mathfrak{F}_{ij}^{T}$ is the set of emission light fluence measured at temperature T. $F_{ij}^{T}(\mu_{af})$ is the set of simulated emission light fluence, which is calculated by solving the forward problem defined by Eq. (1). N_s and N_d, respectively, represent the total number of sources and detectors. The Levenberg-Marquardt method is used to minimize the cost function in Eq. (2), while iteratively updating the vector of unknowns μ_{af} by [55,66,68,72–75]

$$X_{n+1} = X_n + \left(J^T J + \lambda I\right)^{-1} J^T (\mathfrak{F} - F), \tag{3}$$

where X represents the unknown vector of μ_{af} and J is the Jacobian matrix. The reconstructed μ_{af} map at the end of this conventional FT process is a low-resolution one that cannot resolve small or closely located multiple targets. The advantage of the TMFT is the high-resolution binary map it renders with the help of the focused ultrasound and ThermoDots. To obtain a quantitatively accurate fluorophore absorption map, this binary map is incorporated into the FT image reconstruction algorithm as *soft priori*. In summary, a penalty matrix describing the binary mask retrieved using the HIFU is implemented, which can be represented as [37,44,76]

$$L_{ij} = \begin{cases} 0 & i \text{ and } j \text{ not in the same region} \\ -\dfrac{1}{N_r} & i \text{ and } j \text{ in the same region} \\ 1 & i = j \end{cases}, \tag{4}$$

where N_r represents the number of nodes included in each region r. The FT inverse problem is solved again but by implementing the penalty matrix this time. It guides and constrains the solution to yield a high-resolution fluorescence absorption map. In this step, the inverse problem is solved iteratively by updating the unknown μ_{af} using the Levenberg-Marquardt method:

$$X_{n+1} = X_n + \left(J^T J + \lambda L^T L\right)^{-1} J^T (\mathfrak{F} - F). \tag{5}$$

Solving the inverse problem as defined by Eq. (5) significantly improves the quality of the fluorescence images and provides much superior quantitative accuracy, owing to the high resolution of focused ultrasound.

3. RESULTS

To test the performance of our new continuous scanning method based on the ICCD, phantoms simulating tissue optical properties are used. Two different rectangular-shaped (50 × 25 × 17 mm^3) agarose gel phantoms are prepared, Figs. 5(a) and 5(b). Intralipid (0.5%) and India ink are added to the agarose gel to set the absorption and reduced scattering coefficients of the phantom to be 0.01 mm^{-1} and 0.8 mm^{-1}, respectively [77]. To create

a region with the accumulation of ThermoDots within the phantoms, a 10-mm-tall and 3-mm-diameter glass tube is inserted at the center of the first phantom along its z axis. The fluorescence absorption of the ThermoDots is set to 0.26 mm^{-1}. The top side of the tube is located 4 mm below the upper surface of the phantom, Fig. 5(a). The very same tube is placed orthogonally in the middle of the second phantom, Fig. 5(b). While the first phantom allows evaluation of the resolution of the ICCD-based TMFT primarily in the $x - y$ plane, the second one helps determine resolution mainly in the z direction. This is critical since the length of the HIFU focal zone is much bigger than its width, resulting in lower TMFT resolution in the z direction compared to the $x - y$ plane.

A. Phantom I: Inclusion Is Positioned along the z-Axis

As mentioned in the data acquisition section, first, optical absorption tomography measurements are acquired. The averaged recovered optical properties of the phantoms' background are $\mu_a = 0.013\ \ mm^{-1}$ and $\mu_s' = 0.87\ \ mm^{-1}$. Following that, TMFT measurements are performed. The geometry of the phantom shown in Fig. 5(a) is built using the CAD toolbox of COMSOL Multiphysics. Following that, first, a homogenous mesh was generated using the COMSOL meshing toolbox. Only the outer geometry of the phantom is considered, and the maximum element size is set to 0.25 mm. This homogenous mesh has 24,929 tetrahedral elements connected at 4940 nodes. Using conventional FT measurement obtained over the 8×5 grid, fluorescence absorption maps of the ThermoDots (μ_{af}) are reconstructed first without TMFT measurements. As seen in Fig. 6, conventional FT successfully localizes the inclusion very well, but it fails to recover its real size. In fact, the recovered diameter of the inclusion is 8.15 mm while the recovered length is around 13.53 mm. Hence, the recovered volume is much larger than the real volume that results in significant underestimation of the fluorescence absorption of the ThermoDots, 0.051 ± 0.015 mm^{-1}. Consequently, the error in the recovered fluorescence absorption is nearly ~81%. Please note that, to calculate the standard deviation in the recovered values, the image reconstruction process is repeated 5 times with different initial values and regularization parameters.

For TMFT reconstruction, first, another mesh is generated with the same maximum element size. Following that, however, the boundary of the inclusion delineated by the binary map obtained with the HIFU scan is implemented in this mesh. Even prior to any reconstruction process, this HIFU-derived binary mask localizes the inclusion with high accuracy. This binary mask is used as *soft a priori* to solve the FT inverse problem in order to recover the concentration of ThermoDots within the tube with high accuracy [43,44,46,55]. The fluorescence absorption map obtained at the end of TMFT shows its superior spatial resolution and quantitative accuracy compared to the conventional FT, Fig. 6. TMFT nearly recovered the exact diameter of the tube, with a slight overestimation of only 0.7 mm, which might be due to continuous motion of the HIFU beam during the ICCD image acquisition and the result of the interpolation from the mesh to the Cartesian grid image as we demonstrated before [46]. Meanwhile, TMFT recovers fluorescent absorption of the inclusion with high accuracy at 0.241 ± 0.012 mm^{-1}, which represents an error of 7%.

B. Phantom II: Inclusion Is Positioned along the z-Axis

The TMFT binary map resolution directly depends on the HIFU focal spot size. Although the diameter of the HIFU beam is small, its focal depth is much larger in size, around 10 mm. That unfortunately results in poor resolution in the z axis. Since the inclusion is positioned along the z axis, the first phantom mainly evaluates the resolution in x and y axis. To be able to evaluate the resolution of the system in the z axis, a second phantom is prepared. In this phantom, the very same inclusion is positioned along the x axis.

The identical data acquisition procedure is followed for the second phantom. Again, a homogenous mesh is generated using the COMSOL meshing toolbox. The absorption measurements are used to recover the mean absorption and reduced scattering coefficients $\mu_a = 0.012\ \text{mm}^{-1}$ and $\mu_s' = 0.85\ \text{mm}^{-1}$, respectively. Following that, the FT and TMFT measurements are performed. A heterogeneous mesh is prepared considering the inclusion boundaries retrieved from the TMFT HIFU-derived mask for this second phantom. Once again, FT reconstructions are performed with and without the TMFT binary mask.

Figure 7 shows the reconstruction results in different planes. As expected, conventional FT successfully localizes the inclusion well, but it fails to recover its real size. The recovered diameter of the inclusion is 11.5 mm while its length is recovered around 11.8 mm. Consecutively, the fluorescence absorption of the ThermoDots is again drastically underestimated, $0.063 \pm 0.017\text{mm}^{-1}$. This translates to an error in the recovered mean fluorescence absorption of nearly ~76%. On the other hand, TMFT recovered the diameter of the tube much better compared to the conventional FT, 6.78 mm. However, its accuracy is worse than the previous case as expected since the tube is positioned along the x axis, which reveals the poor performance of TMFT in the z direction. The fluorescent absorption of the inclusion is also recovered with higher accuracy with TMFT compared to the conventional FT, $0.10 \pm 0.011\ \text{mm}^{-1}$, with 61% error. However, the overall TMFT quantitative accuracy is not even as close to the first case as well, owing to the long focal depth of the HIFU.

4. CONCLUSION

The new continuous-scan method described in this work is a critical step toward the application of TFMT method for *in vivo* small animal imaging since it reduces the total imaging time for a FOV of $50 \times 25\ \text{mm}^2$ below 30 min. The camera-based design also allows the positioning of animal on a membrane, which provides high throughput for *in vivo* applications together with the fast-scan capability. On top, ThermoDots are optimized for a working range of 30–34°C using a new polymer F108 by our industrial collaborators from InnoSense LLC. This is also another crucial step for small animal imaging with TMFT.

In TMFT, ultrasound provides the high resolution while optical fluorescence imaging delivers the superior sensitivity. Indeed, TMFT relies on the acoustics waves from the focused ultrasound transducer and, therefore, is not constrained by the same scattering and absorption limitations as optical waves. One of the strengths of our technique is that the HIFU transducer has a focal length of 60 mm in tissue, which makes it very suitable for *in vivo* preclinical and clinical applications. Another one is the reduced imaging time since HIFU and laser beam coupling eliminates the requirement of the linear scan from opposite

direction as well as extensive postprocessing required for the case of decoupled beams. It should be noted that, however, the coupling beams do not affect the overall reconstruction quality.

Meanwhile, one weakness of our current setup is the low resolution in the z direction. The focal spot of the HIFU transducer used in our setup is around 1.3 mm. However, the focal depth of the beam is around 10 mm, nearly sevenfold bigger. This is generally true for all HIFU transducers and directly reflects to the distribution of local temperature elevation around the focal spot. Hence, the binary map provided by the TMFT scan has a far better resolution in the $x - y$ plane. To evaluate the resolution in all directions, two different phantoms are utilized in this work. The HIFU-derived binary map is utilized as a soft *a priori*, during the final TMFT reconstruction. In both cases shown above, the error of the conventional FT in the recovered fluorescence absorption is nearly 80%. Compared to the conventional FT, the TMFT reconstruction algorithm manages to recover the inclusion with great accuracy when the HIFU binary map is used to guide and constrain the reconstruction algorithm. When the target is positioned along the z axis, the error in the recovered fluorescence absorption goes down to 7% with TMFT. Unfortunately, the error increases to 60% when the object is positioned along the x axis. This is attributed to the long focal length of the HIFU beam, along the z axis. Although the diameter of the inclusion is 3 mm, the HIFU binary map cannot resolve it since the HIFU focal length is 10 mm. That leads to a larger area delineated by this binary map and, hence, incorrect *a priori* information that resulted in poor resolution and low accuracy. Since the HIFU binary map cannot provide adequate high-resolution information along the z axis, the results are heavily weighted by the FT resolution in this direction. Although FT is operating in limited angle tomography mode, i.e., illumination is from the bottom and detection is from the top, the high number of source-detector configuration based on the high number of ICCD pixels allows delineating the size of the inclusion along the z axis better than the HIFU binary map alone. Here the inclusion is placed either parallel or perpendicular to the z axis to show the best and worst cases. If it was placed at an angle, again similar results would be obtained—the resolution in the z axis would be much worse but compensated with the FT up to a certain level. Although the FT counterpart acquires 2D fluorescence images, a total of 40 images are acquired for different source positions (8×5 grid), and that provides ample source-detector pairs (any source position x number of pixels in a 2D image) for a good 3D reconstruction.

A solution to improve the performance of TMFT in the z-direction and bring it to the same level in the $x - y$ plane might be utilizing more than one HIFU transducer. Our conceptual design for the next generation TMFT will be placing two HIFU transducers orthogonally to send the HIFU beams at 45° and —45° to the animal sequentially. Both HIFU transducers will be positioned at the bottom of the animal and scanned with translational stages similar to the current design. Since the HIFU beams will be turned on sequentially, the scan time will double, but the cross-section area of the binary maps obtained with each HIFU beam will be much smaller compared to their individual focal length. Prior to this technically challenging improvement, our next aim will be making the ThermoDots disease-targeting using antibodies. Currently, their fast pharmacokinetics (i.e., wash-in and wash-out in a tumor model within a couple of minutes) does not give enough time for imaging. Making

them disease-targeting will allow ThermoDots to stay in the target area for a long time and permit TMFT imaging *in vivo*.

There is a great interest in the development of disease-targeting fluorescent contrast agents in the clinical arena. For example, the first ovarian-cancer-targeting fluorescent agent has been recently approved by the FDA [78]. Used in tandem with intraoperative fluorescence cameras, this agent will soon be a part of the routine clinical practice to help physicians during ovarian cancer debulking surgery. With the advent of these clinical smart cancer-targeting probes, demand for higher resolution and quantitatively accurate fluorescent small animal imaging will increase, particularly for more realistic orthotopic tumor models. Therefore, TMFT is expected to play an important role in the development of new smart fluorescence probes targeting different tumor types or diseased tissue in the near future.

Funding.

National Institutes of Health (HHSN261201300068C, P30CA62203, R01EB008716, R21CA170955, R21CA191389, R33CA120175); Susan G. Komen North Carolina (KG101442).

Data availability.

Data underlying the results presented in this paper are not publicly available at this time but may be obtained from the authors upon reasonable request.

REFERENCES

1. Bremer C, Ntziachristos V, and Weissleder R, “Optical-based molecular Imaging: contrast agents and potential medical applications,” Eur. Radiol 13, 231–243 (2003). [PubMed: 12598985]
2. Ntziachristos V, Bremer C, Graves EE, et al. , “In vivo tomographic imaging of near-infrared fluorescent probes,” Mol. Imaging 1, 82–88 (2002). [PubMed: 12920848]
3. Urano Y, Asanuma D, Hama Y, et al. , “Selective molecular imaging of viable cancer cells with pH-activatable fluorescence probes,” Nat. Med 15, 104–109 (2009). [PubMed: 19029979]
4. von Burstin J, Eser S, Seidler B, et al. , “Highly sensitive detection of early-stage pancreatic cancer by multimodal near-infrared molecular imaging in living mice,” Int. J. Cancer 123, 2138–2147 (2008). [PubMed: 18709639]
5. Sosnovik DE, Nahrendorf M, Deliolanis N, et al. , “Fluorescence tomography and magnetic resonance imaging of myocardial macrophage infiltration in infarcted myocardium in vivo,” Circulation 115, 1384–1391 (2007). [PubMed: 17339546]
6. Nahrendorf M, Sosnovik DE, Waterman P, et al. , “Dual channel optical tomographic imaging of leukocyte recruitment and protease activity in the healing myocardial infarct,” Circ. Res 100, 1218–1225 (2007). [PubMed: 17379832]
7. Kobayashi H, Koyama Y, Barrett T, et al. , “Multimodal nanoprobes for radionuclide and five-color near-infrared optical lymphatic imaging,” ACS Nano 1, 258–264 (2007). [PubMed: 19079788]
8. Aikawa E, Nahrendorf M, Figueiredo JL, et al. , “Osteogenesis associates with inflammation in early-stage atherosclerosis evaluated by molecular imaging in vivo,” Circulation 116, 2841–2850 (2007). [PubMed: 18040026]
9. Cunha L, Horvath I, Ferreira S, et al. , “Preclinical imaging: an essential ally in modern biosciences,” Mol. Diagn. Ther 18, 153–173 (2014). [PubMed: 24146172]
10. Leblond F, Davis SC, Valdes PA, et al. , “Pre-clinical whole-body fluorescence imaging: review of instruments, methods and applications,” J. Photochem. Photobiol. B 98, 77–94 (2010). [PubMed: 20031443]

11. Ntziachristos V, Turner G, Dunham J, et al. , “Planar fluorescence imaging using normalized data,” J. Biomed. Opt 10, 064007 (2005).
12. Wang D, Zhang H, Vu T, et al. , “Trans-illumination intestine projection imaging of intestinal motility in mice,” Nat. Commun 12, 1682 (2021). [PubMed: 33727562]
13. Cano P, Godoy A, Escamilla R, et al. , “Stromal-epithelial cell interactions and androgen receptor-coregulator recruitment is altered in the tissue microenvironment of prostate cancer,” Cancer Res. 67, 511–519 (2007). [PubMed: 17234758]
14. Chrenek MA, Wong P, and Weaver VM, “Tumour-stromal interactions. Integrins and cell adhesions as modulators of mammary cell survival and transformation,” Breast Cancer Res. 3, 224–229 (2001). [PubMed: 11434873]
15. Schmeichel KL, Weaver VM, and Bissell MJ, “Structural cues from the tissue microenvironment are essential determinants of the human mammary epithelial cell phenotype,” J. Mammary Gland Biol. Neoplasia 3, 201–213 (1998). [PubMed: 10819528]
16. Talmadge JE, Singh RK, Fidler IJ, et al. , “Murine models to evaluate novel and conventional therapeutic strategies for cancer,” Am. J. Pathol 170, 793–804 (2007). [PubMed: 17322365]
17. Killion JJ, Radinsky R, and Fidler IJ, “Orthotopic models are necessary to predict therapy of transplantable tumors in mice,” Cancer Metastasis Rev. 17, 279–284 (1998). [PubMed: 10352881]
18. Kepshire D, Mincu N, Hutchins M, et al. , “A microcomputed tomography guided fluorescence tomography system for small animal molecular imaging,” Rev. Sci. Instrum 80, 043701 (2009).
19. Davis SC, Pogue BW, Springett R, et al. , “Magnetic resonance-coupled fluorescence tomography scanner for molecular imaging of tissue,” Rev. Sci. Instrum 79, 064302 (2008).
20. Lin Y, Barber WC, Iwanczyk JS, et al. , “Quantitative fluorescence tomography using a trimodality system: in vivo validation,” J. Biomed. Opt 15, 040503 (2010).
21. Josiah DG, Akshat P, Hamid G, et al., “High-frequency ultrasound-guided fluorescence tomography of protoporphyrin IX in subcutaneous tumors,” in Biomedical Optics and 3-D Imaging (Optical Society of America, 2010), paper BMB5.
22. Gruber JD, Paliwal A, Krishnaswamy V, et al. , “System development for high frequency ultrasound-guided fluorescence quantification of skin layers,” J. Biomed. Opt 15, 026028 (2010).
23. Nouizi F, Brooks J, Zuro DM, et al. , “Development of a theranostic preclinical fluorescence molecular tomography/cone beam CT-guided irradiator platform,” Biomed. Opt. Express 13, 6100–6112 (2022). [PubMed: 36733750]
24. Nouizi F, Brooks J, Zuro DM, et al. , “Implementation of a combined theranostic x-ray irradiator/fluorescence imaging system for automatic assessment of tumor vascular response to radiation therapy,” Proc. SPIE 11944, 15–19 (2022).
25. Nouizi F, Brooks J, Zuro DM, et al. , “Theranostic fluorescence tomography-guided small animal x-ray irradiator platform: system development and validation,” in Optical Tomography and Spectroscopy (Optica, 2022), paper OTu2D.7.
26. Li S, Zhang M, and Zhu Q, “Ultrasound segmentation-guided edge artifact reduction in diffuse optical tomography using connected component analysis,” Biomed. Opt. Express 12, 5320–5336 (2021). [PubMed: 34513259]
27. Uddin KMS, Mostafa A, Anastasio M, et al. , “Two step imaging reconstruction using truncated pseudoinverse as a preliminary estimate in ultrasound guided diffuse optical tomography,” Biomed. Opt. Express 8, 5437–5449 (2017). [PubMed: 29296479]
28. Zhang M, Xue M, Li S, et al. , “Fusion deep learning approach combining diffuse optical tomography and ultrasound for improving breast cancer classification,” Biomed. Opt. Express 14, 1636–1646 (2023). [PubMed: 37078047]
29. Zhoua L, Yazicia B, and Ntziachristosb V, “Fluorescence molecular-tomography reconstruction with a priori anatomical information,” Proc. SPIE 6868, 68680O (2008).
30. Yuan B,Liu Y, Mehl PM et al. , “Microbubble-enhanced ultrasound-modulated fluorescence in a turbid medium,” Appl. Phys. Lett 95, 181113(2009).
31. Kobayashi M, Mizumoto T, Shibuya Y, et al. , “Fluorescence tomography in turbid media based on acousto-optic modulation imaging,” Appl. Phys. Lett 89, 181102 (2006).
32. Yuan B. and Liu Y, “Ultrasound-modulated fluorescence from rhodamine B aqueous solution,” J. Biomed. Opt 15, 021321 (2010).

33. Schutt C, “Ultrasound-modulated fluorescent contrast agent for optical imaging through turbid media,” Proc. SPIE 8165, 81650B (2011).
34. Yuan B, “Ultrasound-modulated fluorescence based on a fluorophore-quencher-labeled microbubble system,” J. Biomed. Opt 14, 024043 (2009).
35. Klibanov AL, “Ligand-carrying gas-filled microbubbles: ultrasound contrast agents for targeted molecular imaging†,” Bioconjugate Chem. 16, 9–17 (2004).
36. Takalkar AM, Klibanov AL, Rychak JJ, et al. , “Binding and detachment dynamics of microbubbles targeted to P-selectin under controlled shear flow,” J. Control. Release 96, 473–482 (2004). [PubMed: 15120903]
37. Lin Y, “Temperature modulated fluorescence tomography in a turbid media,” Appl. Phys. Lett 100, 073702 (2012).
38. Lin Y, Bolisay L, Kwong T, et al. , “Temperature modulated fluorescence tomography based on both concentration and lifetime contrast,” J. Biomed. Opt 17, 056007 (2012).
39. Kwong TC, Nouizi F, Lin Y, et al. , “Temperature-modulated fluorescence tomography: modulating tissue temperature using HIFU for high-resolution in vivo fluorescence tomography,” Proc. SPIE 8574, 857405 (2013).
40. Nouizi F, Kwong T, Lin Y, et al., “A combined HIFU-fluorescence tomography high-resolution imaging technique using temperature-modulated thermodots,” in Optics in the Life Sciences (Optica Publishing Group, 2013), paper JW3B.8.
41. Kwong TC, Nouizi F, Lin Y, et al. , “Validation of temperature-modulated fluorescence tomography in vivo,” Proc. SPIE 8937, 89370H (2014).
42. Tiffany FN, Kwong C, Sampathkumaran U, et al. , “Activatable thermo-sensitive ICG encapsulated pluronic nanocapsules for temperature sensitive fluorescence tomography,” Proc. SPIE 9339, 93390C (2015).
43. Lin Y, Nouizi F, Kwong TC, et al. , “Simulation-based evaluation of the resolution and quantitative accuracy of temperature-modulated fluorescence tomography,” Appl. Opt 54, 7612–7621 (2015). [PubMed: 26368884]
44. Nouizi F, Kwong TC, Cho J, et al. , “Implementation of a new scanning method for high-resolution fluorescence tomography using thermo-sensitive fluorescent agents,” Opt. Lett 40, 4991–4994 (2015). [PubMed: 26512501]
45. Kwong TC, Nouizi F, Lin Y, et al. , “Thermal outlining using focused ultrasound (TOFU) with reversible temperature sensitive fluorescent probes,” Proc. SPIE 9701, 97010L (2016).
46. Kwong TC, Nouizi F, Lin Y, et al. , “Experimental evaluation of the resolution and quantitative accuracy of temperature-modulated fluorescence tomography,” Appl. Opt 56, 521–529 (2017). [PubMed: 28157909]
47. Yongping C. and Xingde L, “Thermo/pH-responsive and reversible NIR fluorescent probes for optical molecular imaging,” in Biomedical Optics and 3-D Imaging (Optical Society of America, 2010), paper JMA105.
48. Kim TH, Chen Y, Mount CW, et al. , “Evaluation of temperature-sensitive, indocyanine green-encapsulating micelles for noninvasive near-infrared tumor imaging,” Pharm. Res 27, 1900–1913 (2010). [PubMed: 20568000]
49. Nouizi F, Kwong TC, Ruiz J, et al. , “A thermo-sensitive fluorescent agent based method for excitation light leakage rejection for fluorescence molecular tomography,” Phys. Med. Biol 64, 035007 (2018).
50. Nouizi F, Kwong TC, Kwong J, et al. , “Excitation light leakage suppression using temperature sensitive fluorescent agents,” Proc. SPIE 9319, 93190Y (2015).
51. Yuan B, Uchiyama S, Liu Y, et al. , “High-resolution imaging in a deep turbid medium based on an ultrasound-switchable fluorescence technique,” Appl. Phys. Lett 101, 033703 (2012).
52. Zhao J, Zhong D, and Zhou S, “NIR-l-to-NIR-ll fluorescent nanomaterials for biomedical imaging and cancer therapy,” J. Mater. Chem. B 6, 349–365 (2018). [PubMed: 32254515]
53. Pei Y, Wei MY, Cheng B, et al. , “High resolution imaging beyond the acoustic diffraction limit in deep tissue via ultrasound-switchable NIR fluorescence,” Sci. Rep 4, 4690 (2014). [PubMed: 24732947]

54. Cheng B, Bandi V, Wei MY, et al. , “High-resolution ultrasound-switchable fluorescence imaging in centimeter-deep tissue phantoms with high signal-to-noise ratio and high sensitivity via novel contrast agents,” PLoS One 11, e0165963 (2016).
55. Kwong TC, Nouizi F, Cho J, et al. , “Feasibility study of high spatial resolution multimodality fluorescence tomography in ex vivo biological tissue,” Appl. Opt 56, 7886–7891 (2017). [PubMed: 29047774]
56. Nouizi F, Erkol H, Nikkhah D, et al. , “Development of a preclinical CCD-based temperature modulated fluorescence tomography platform,” Biomed. Opt. Express 13, 5740–5752 (2022). [PubMed: 36733748]
57. Mehrabi M, Nouizi F, Algarawi M, et al. , “CCD-based temperature modulated fluorescence tomography,” Proc. SPIE 1087, 108740Y (2019).
58. Nikkhah D, Nouizi F, Hurtado R, et al. , “Temperature modulated fluorescence tomography feasibility using an intensified CCD camera,” in Optics and the Brain (Optica, 2022), paper JM3A.9.
59. Liu RL and Cai RQ, “Recent advances in ultrasound-controlled fluorescence technology for deep tissue optical imaging,” J. Pharm. Anal 12, 530–540 (2022). [PubMed: 36105171]
60. Cheng B, Bandi V, Yu S, et al. , “The mechanisms and biomedical applications of an NIR BODIPY-based switchable fluorescent probe,” Int. J. Mol. Sci 18, 384 (2017). [PubMed: 28208666]
61. Liu R, Yao T, Liu Y, et al. , “Temperature-sensitive polymeric nanogels encapsulating with beta-cyclodextrin and ICG complex for high-resolution deep-tissue ultrasound-switchable fluorescence imaging,” Nano Res. 13, 1100–1110 (2020).
62. Pei Y. and Wei M, “Newly-engineered materials for bio-imaging technology: a focus on the hybrid system of ultrasound and fluorescence,” Front. Bioeng. Biotechnol 7, 88 (2019). [PubMed: 31080797]
63. Liu Y, Yao T, Cai W, et al. , “A biocompatible and near-infrared liposome for in vivo ultrasound-switchable fluorescence imaging,” Adv. Healthc Mater 9, 1901457 (2020).
64. Zhang Q, Morgan SP, and Mather ML, “Nanoscale ultrasound-switchable FRET-based liposomes for near-infrared fluorescence imaging in optically turbid media,” Small 13, 1602895 (2017).
65. Lin Y, Barber WC, Iwanczyk JS, et al. , “Quantitative fluorescence tomography using a combined tri-modality FT/DOT/XCT system,” Opt. Express 18, 7835–7850 (2010). [PubMed: 20588625]
66. Arridge S, “Optical tomography in medical imaging,” Inverse Probl. 15, R41–R93 (1999).
67. Nouizi F, Erkol H, Luk A, et al. , “An accelerated photo-magnetic imaging reconstruction algorithm based on an analytical forward solution and a fast Jacobian assembly method,” Phys. Med. Biol 61, 7448–7465 (2016). [PubMed: 27694717]
68. Nouizi F, Luk A, Thayer D, et al. , “Experimental validation of a high-resolution diffuse optical imaging modality: photomagnetic imaging,” J. Biomed. Opt 21, 016009 (2016).
69. Nouizi F, Erkol H, Luk A, et al. , “Real-time photo-magnetic imaging,” Biomed. Opt. Express 7, 3899–3904 (2016). [PubMed: 27867701]
70. Erkol H, Nouizi F, Unlu MB, et al. , “An extended analytical approach for diffuse optical imaging,” Phys. Med. Biol 60, 5103–5121 (2015). [PubMed: 26083326]
71. Nouizi F, Chabrier R, Torregrossa M, et al., “3D modeling for solving forward model of no-contact fluorescence diffuse optical tomography method,” in Diffuse Optical Imaging II„ Cubeddu R. and Hielscher A, eds., Vol. 7369 of Proceedings of SPIE-OSA Biomedical Optics, (Optica Publishing Group, 2009), paper 7369_0C.
72. Nouizi F, Torregrossa M, Chabrier R, et al. , “Improvement of absorption and scattering discrimination by selection of sensitive points on temporal profile in diffuse optical tomography,” Opt. Express 19, 12843–12854 (2011). [PubMed: 21716527]
73. Levenberg K, “A method for the solution of certain non-linear problems in least squares,” Quart. Appl. Math 2, 164–185 (1944).
74. Marquardt DW, “An algorithm for least-squares estimation of non-linear parameters,” J. Soc. Indus. Appl. Math 11, 431–441 (1963).
75. Nouizi F, Erkol H, Luk A, et al., “Analytical photo magnetic imaging,” in Optical Tomography and Spectroscopy (Optical Society of America, 2016), paper OW4D.7.

76. Yalavarthy BPP, Dehghani H, Carpenter C, et al. , “Structural information within regularization matrices improves near infrared diffuse optical tomography,” Opt. Express 15, 8043–8058 (2007). [PubMed: 19547132]

77. Wan W, Wang Y, Qi J, et al. , “Region-based diffuse optical tomography with registered atlas: in vivo acquisition of mouse optical properties,” Biomed. Opt. Express 7, 5066–5080 (2016). [PubMed: 28018725]

78. Tanyi JL, Randall LM, Chambers SK, et al. , “A phase III study of pafolacianine injection (OTL38) for intraoperative imaging of folate receptor-positive ovarian cancer (Study 006),” J. Clin. Oncol 41, 276–284 (2023). [PubMed: 36070540]

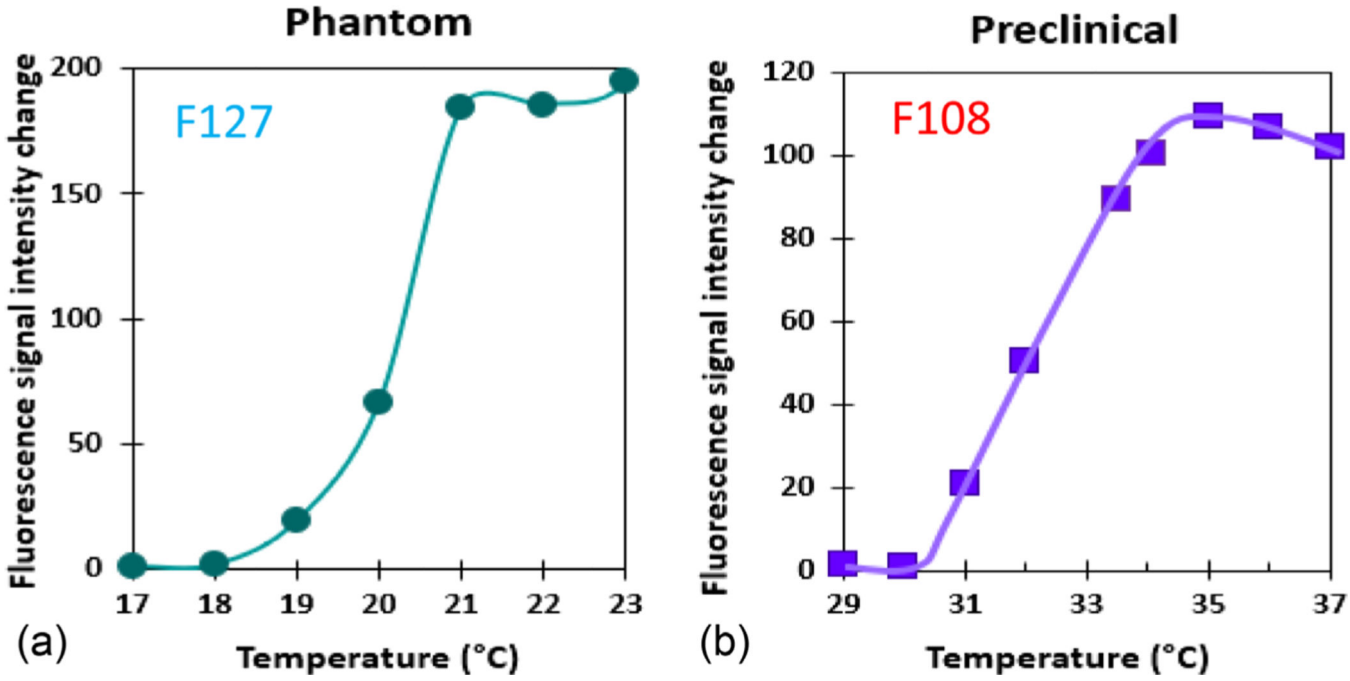

Fig. 1.

Temperature response of the ThermoDots designed for: (a) phantom (17–23°C), and (b) preclinical (29–37°C) studies using polymers F127 and F108, respectively.

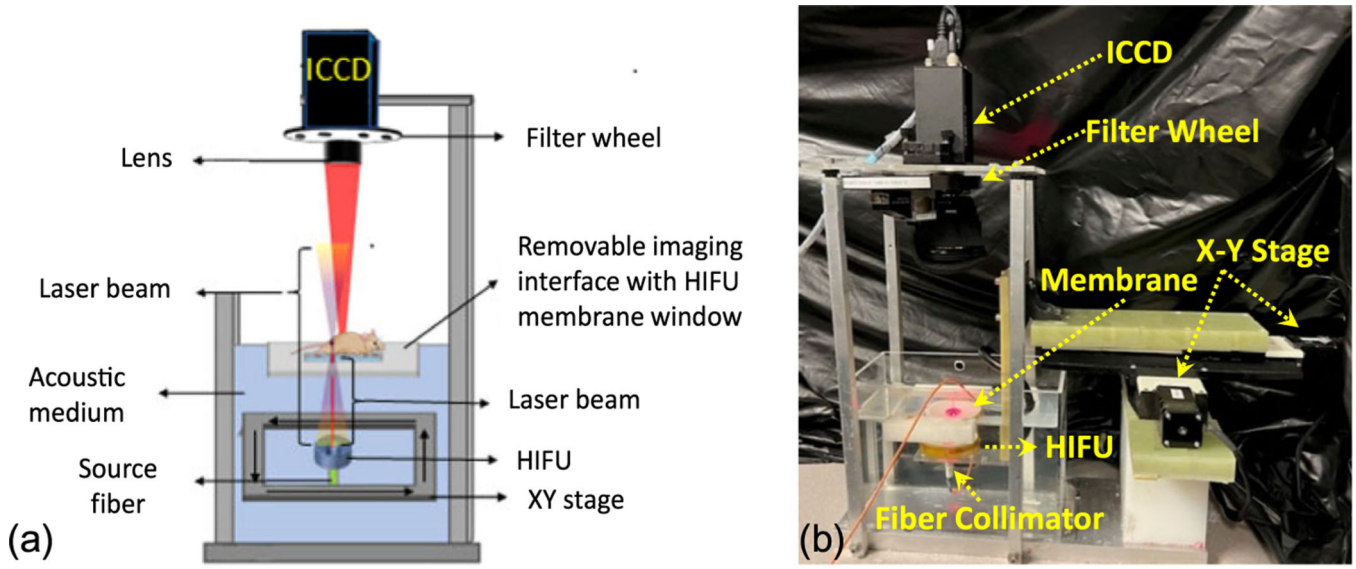

Fig. 2.

(a) Schematic of the *in vivo* small animal TMFT system. (b) photo of the TMFT prototype.

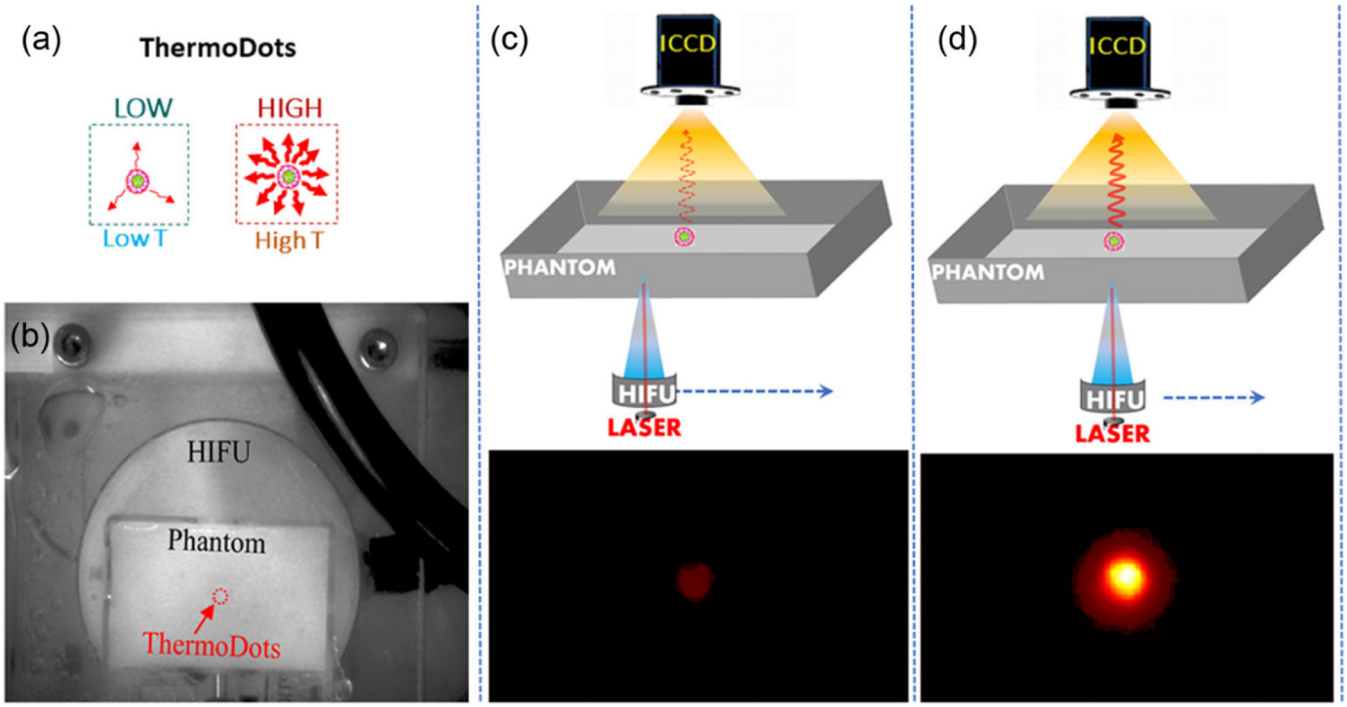

Fig. 3.

(a) Florescence emission of the ThermoDots is low at low temperatures; however, it goes up with the local temperature. (b) Room light photo taken by the ICCD that shows the phantom and HIFU transducer underneath. The HIFU cable is visible (black) on the right-hand side. The position of the ThermoDots is indicated by the red circle. (c) and (d) Schematic of the system, while the HIFU and laser beams are scanned together over the phantom. ICCD detects (c) low fluorescence signal when ThermoDots are out of the ultrasound focal zone and (d) high fluorescence signal when they are within it.

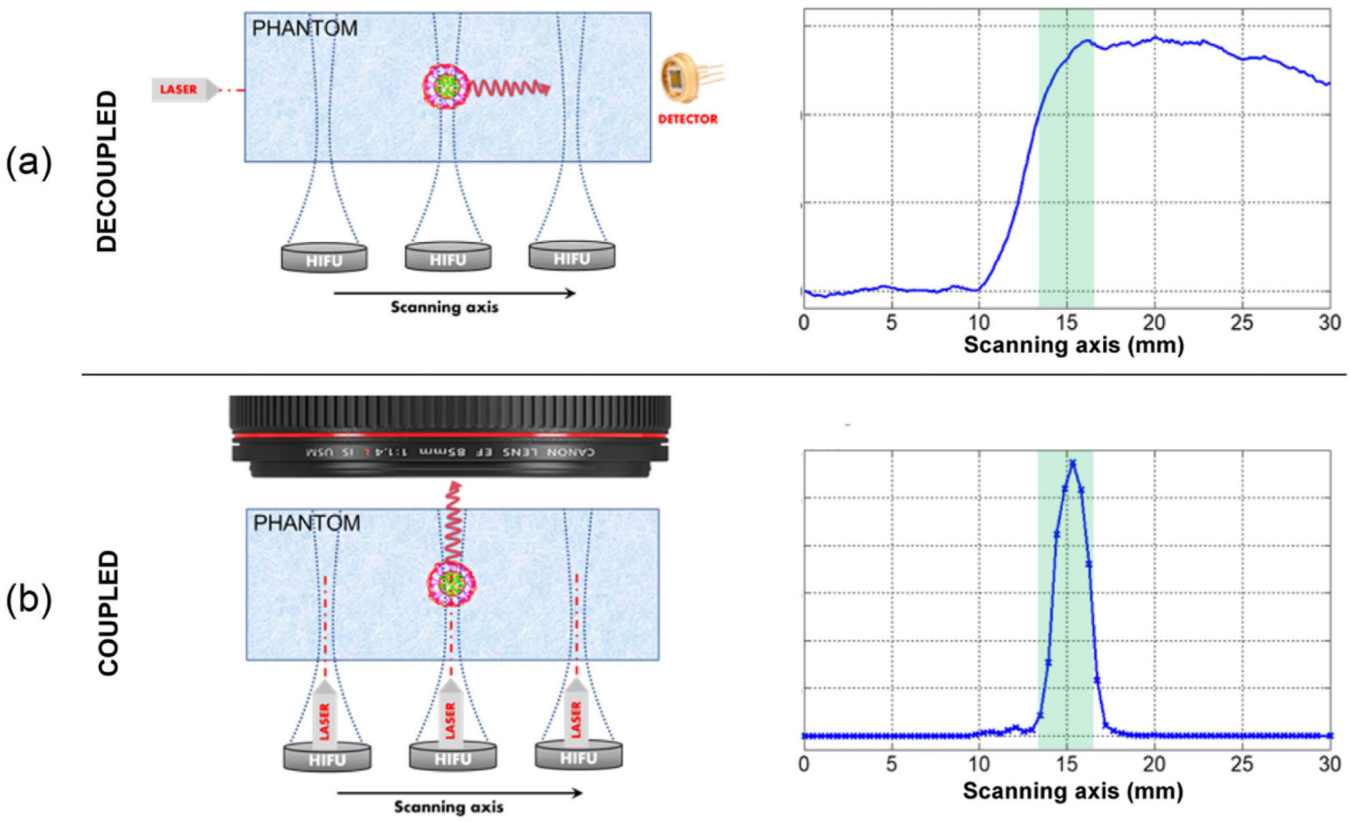

Fig. 4.

Comparison of coupled and decoupled HIFU and laser beams. (a) When decoupled, the emission signal of ThermoDots stays high for a long time due to elevated local temperature, which makes delineating object boundary (green area) harder in one pass. (b) When coupled, scanning only in one direction is enough to determine the object boundary. The green highlighted area shows the position of the 3-mm-diameter target filled with ThermoDots.

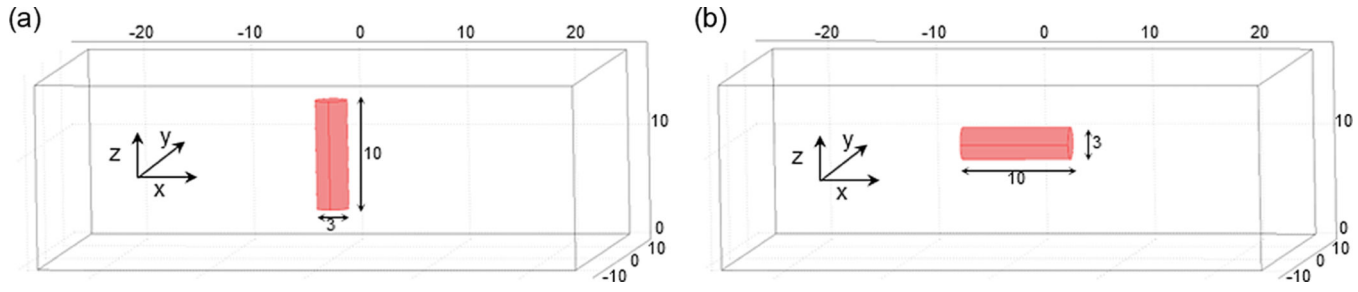

Fig. 5.

Schematics of the 50 × 30 × 17 mm^3 rectangular agar phantoms used in the evaluation studies. A 3-mm-diameter and 10-mm-height glass tube filled with ThermoDots is inserted at the center of these two phantoms (a) along its *z* axis and (b) along its *x* axis respectively.

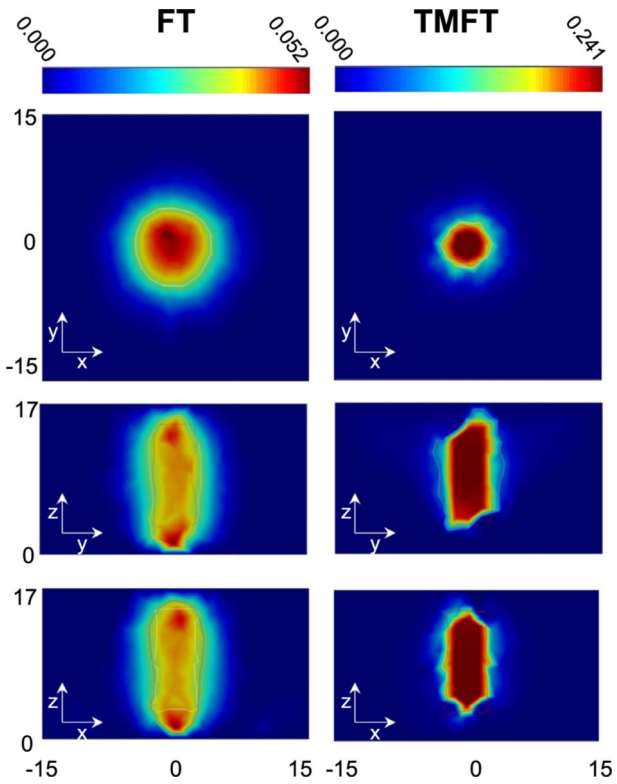

Fig. 6.

Reconstructed 3D fluorescence absorption images segmented at full width at half-maximum with conventional FT (left column) and TMFT (right column). Each row shows the images in different planes ($x - y$, $y - z$, and $x - z$). The real boundary of the inclusion is represented with black line while the contour of the recovered inclusion is indicated by white lines in each image. It is easily seen in the images that TMFT not only localizes the object much better owing to the HIFU scan but also recovers the mean fluorescence absorption with high accuracy, around 7% error.

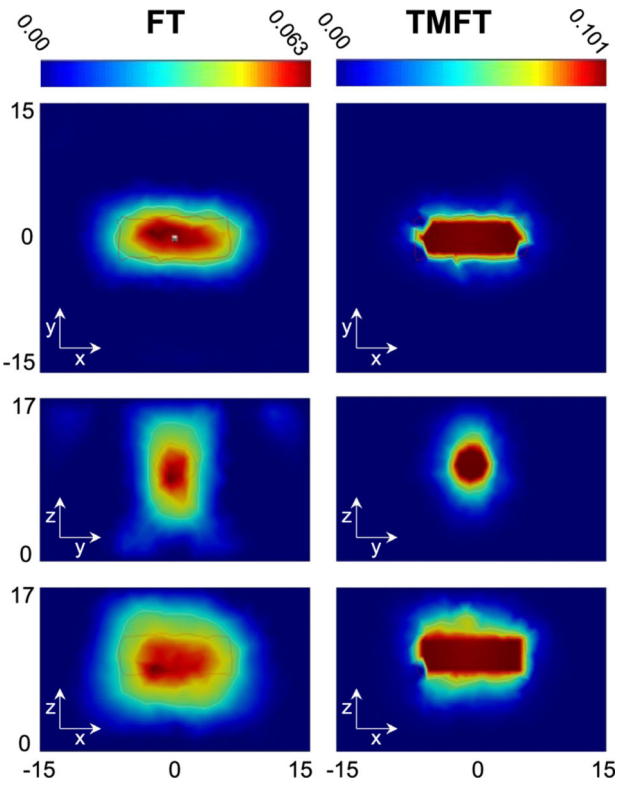

Fig. 7.

Reconstructed 3D fluorescence absorption images segmented at full width at half-maximum with conventional FT (left column) and TMFT (right column). For the second phantom. Each row shows the images in different planes ($x - y$, $y - z$, and $x - z$). The real boundary of the inclusion is represented with black line while the contour of the recovered inclusion is indicated by white lines in each image. TMFT not only localizes the object much better owing to the HIFU scan but also recovers the mean fluorescence absorption with a bit higher accuracy. TMFT accuracy is much worse compared to the first case though, due to long focal depth of the HIFU.